Preprint Title	Zayedene: Carbon sp chains in diamond nanocavities
Authors	Francesco Delodovici, Daniel S. Choi, Mohamed Al Fahim, Larry A. Burchfield and Nicola Manini
Publication Date	11 Jul 2019
Article Type	Full Research Paper
Supporting Information File 1	C6_zayedene.exyz; 7.5 KB
ORCID® iDs	Francesco Delodovici - https://orcid.org/0000-0003-1954-9039; Nicola Manini - https://orcid.org/0000-0003-4374-6374

Zayedene: Carbon *sp* chains in diamond nanocavities

Francesco Delodovici*[1], Daniel S. Choi[2], Mohamed Al Fahim[3], Larry A. Burchfield[4] and Nicola Manini*[5]

Address: [1]Dipartimento di Fisica, Università degli Studi di Milano, Via Celoria 16, 20133 Milano, Italy; [2]Department of Mechanical Engineering, Khalifa University of Science and Technology, P.O. Box 127788, Abu Dhabi, UAE; [3]Alfields, Inc. PO Box 4597, West Richland, WA 99353, USA; [4]Alfields, Inc. PO Box 4597, West Richland, WA 99353, USA and [5]Dipartimento di Fisica, Università degli Studi di Milano, Via Celoria 16, 20133 Milano, Italy

Email: Francesco Delodovici - francesco.delodovici@unimi.it; Nicola Manini - E-mail: nicola.manini@unimi.it

* Corresponding author

Abstract

We propose a new class of carbon allotropes obtained by combining linear *sp* carbon chains with sp^3 bulk carbon. The structure of these crystalline carbon allotropes consists of *sp* chains inserted in cylindrical cavities periodically arranged in hexagonal diamond (lonsdaleite). We carry out a detailed computational analysis of the structural, electronic, and vibrational properties of a simple form in this class: a single C_6 strand embedded in a nm-sized cavity. We obtain a metallic allotrope exhibiting characteristic high-frequency vibrations associated with the *sp* chains stretching modes, and characterized by long-time room-temperature stability. In addition, we suggest how numerous similar allotropes could be constructed within this class, that we call zayedene, all characterized by comparable metallicity and high-frequency vibrations.

Keywords

carbon allotropes; hexagonal diamond; nanocavities; nanotechnologies; *sp*-chains.

Introduction

Linear *sp* carbon chains (SPCCs) are viewed as promising materials for a number of applications in nanomechanics and nanoelectronic/spintronic devices [1-8]. Current research has investigated the structural, electronic, transport, and mechanical properties of linear acetylenic carbon [1,9-22]. In particular SPCCs have usually been investigated mainly in connection with sp^2 carbon [3,7,19, 21,23,24], consistently e.g. with experiments where SPCCs form in the latest stages of graphene breaking under strain [4,25].

In the present work we explore the alternative possibility of combining SPCCs with sp^3 carbon. As SPCCs are highly unsaturated, they tend to react easily with other carbon forming extra bonds, with the result of degrading into sp^2 or sp^3 structures. For this reason, it is necessary to isolate SPCCs in some sufficiently large cavity inside sp^3 carbon. Such a cavity needs to be, on one hand, long enough to accommodate a SPCC without too much strain and, on the other hand, wide enough to keep the SPCC isolated and prevent spontaneous reaction and degrading. Our choice falls on hexagonal diamond (lonsdaleite), precisely because of its hexagonal structure, which suggests a natural direction for the cavity long axis, although we see no special reason why the same kind of modeling could not be replicated in the context of regular cubic diamond, or some other sp^3 allotrope. In real conditions several types of cavity could coexist, each of them including one or several SPCCs, giving rise to both periodic or disordered distributions of these inclusions. To take advantage of lattice periodicity, we investigate a basic structure constructed as bulk hexagonal diamond spotted with a regular array of identical cavities, each of which holding the same number of SPCCs (typically one). The volume and the shape of these cavities play a central role in the possibility of holding one or more SPCCs inside: a reduced volume or a jagged surface would limit the stability and the maximum possible length of the SPCCs. We propose to name the resulting class of carbon allotropes: *zayedenes*, after Sheik Zayed bin Sultan Al Nahyan, the first President of the United Arab Emirates. The genesis of this proposed new class of allotropes began with a simple "ball & stick" model proposed in 2017 by two of our team members: Al Fahim & Burchfield.

The model

For the basic building blocks we take an appropriate number of carbon lonsdaleite primitive units repeated periodically along the primitive vectors. From this block we construct a cylindrical cavity by removing all atoms that fall inside a cylinder (lightly shaded region of Figure 1), with the symmetry axis parallel to the **c** primitive vector of hexagonal diamond.

The cylinder is placed in a way that the bottom and top C atoms along the cylinder axis stick out toward the inside of the cavity with their dangling bonds. We then insert one SPCC (red-highlighted atoms of Figure 1) along the cylinder axis, making sure that the SPCC ends attach to two lonsdaleite dangling bonds inside the cavity. This overall structure, repeated periodically with a primitive cell equaling a supercell consisting of multiple lonsdaleite primitive cells, allows one to address a broad variety of cavity sizes and placements of the SPCC. Appendix A reports alternative less symmetric arrangements of the SPCC in the cavity.

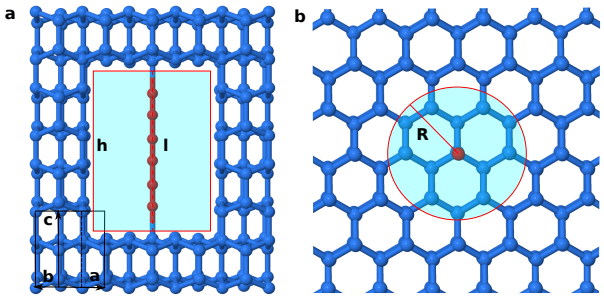

Figure 1: An example of the proposed structure combining sp (red) and sp^3 (blue) carbon. **a**: A side cut in the $\hat{x} - \hat{z}$ plane; one primitive cell of bulk lonsdaleite is highlighted in black. **b**: A top cut in the $\hat{x} - \hat{y}$ plane, showing the circular base of the cylinder (radius $r = 300$ pm) used to cut out the lonsdaleite atoms and construct the cavity. The C_6 SPCC binds to carbons of the sp^3 cage where dangling bonds stick out inside the cavity.

The optimal chain length that fits the cavity axis is clearly related to the height h of the cylinder. Indeed, a chain much shorter than h would be too strongly strained to bind to both top and bottom sides of the cavity. In contrast, a chain significantly longer than h would suffer compressive strain and therefore buckle [26], to the extent that it may even recombine with the lonsdaleite cage. Clearly this latter eventuality depends sensitively on the cavity radius and the atomic-scale roughness of the cavity inner surfaces.

Table 1 collects the information necessary to characterize the length matching between the SPCC and the cavity. An integer m counts the number of vertically-repeated lonsdaleite units cells removed to form the cavity. The resulting cavity height is $h = m \cdot c + b$, in terms of the length $c = 412$ pm of the **c** primitive vector, and of the length $b = 154$ pm of one vertical C-C bond of lonsdaleite [27,28].

The ends of the SPCC chains are linked with the cavity at the top and bottom layer of sp^3-hybridized carbon via single bonds. As a consequence, we expect the carbon chain to display a sizable bond-length alternation , i.e. to be in a polyynic (as opposed to cumulenic) state [12,29]. Typical lengths of the triple and single bonds are $b_t \simeq 121$ pm and $b_s \simeq 133$ pm [11,26]. Accordingly, the length of a N-atoms SPCC is expected to be $l \simeq N \cdot (b_t + b_s)/2 + b_s$. Based on these observations, we can approximately predict the axial strain state of the SPCC by comparing l with h. This comparison is provided in Table 1 for a few well-matching combinations. The fractional strain $\varepsilon = (h-l)/l$ could be as small as $\simeq 0.4\%$ for a $N = 26$ atoms SPCC inserted in a $m = 8$ cavity. As illustrated in Table 1, C_6 and C_{12} experience a significant tensile strain whereas C_{10} is under moderate compressive strain. Of course the stresses associated with these strains could partly be released once these initial idealized structures are allowed to relax.

Table 1: A comparison between a few possible heights h of the cylindrical cavity and the length l of the best-fitting SPCC. m is the number of lonsdaleite c units defining the cavity height, and N is the number of atoms in the SPCC, see Figure 1. The last column reports the nominal fractional strain $\varepsilon = (h-l)/l$ in percent.

m	**h** [pm]	**N**	**l** [pm]	ε [%]
2	978	6	895	9.3
3	1390	10	1403	-0.9
4	1802	12	1657	8.7
5	2214	16	2165	2.2
6	2626	20	2673	-1.7
7	3038	22	2927	3.7
8	3450	26	3435	0.4

To construct a well-defined model for simulations, we need to set the cavity radius R, and the numbers m_c and m_a of repeated lonsdaleite units in the vertical **c** stacking and in the horizontal xy plane, respectively. To prevent a cavity in one periodically repeated block to get too close (or even

worst to interpenetrate) neighboring cavities, the following inequalities must be respected:

$$m_c > m, \tag{1}$$

$$m_a a > 2R + t_{cage}, \tag{2}$$

where $a = 251$ pm is the lonsdaleite lattice spacing in the xy plane, and $t_{cage} = 72$ pm is the minimum acceptable thickness of the cage, which is the length of a single C-C bond projected in the horizontal plane. At the same time, R must exceed a few Å in order to allow longer SPCCs to buckle or to vibrate like violin strings without immediately binding to the cavity inner surface. Given these conditions, the model involves a total number of atoms

$$N_{\rm tot} = 4 m_a^2 m_c + N - N_{\rm cyl}, \tag{3}$$

enclosed in a periodically repeated cell of volume $3^{1/2} 2^{-1} m_a^2 m_c a^2 c$. In Eq. (3), the number of atoms removed from the cavity cylindrical volume is

$$N_{\rm cyl} \simeq \frac{8\pi}{\sqrt{3}} \left(\frac{R}{a}\right)^2 m, \tag{4}$$

where the $\simeq$ symbol indicates that this estimation needs to be rounded to a near integer, depending on which atoms near the cylindrical surface are counted in or out. With 4 valence electrons per carbon atom, the total number of electrons per simulation cell amounts to $4N_{\rm tot}$.

Numeric simulations

Several of the structures resulting from different choices of m_a, m_c, R, m, and N compatible with the conditions (1) and (2) would be worth investigating. However, due to the rapid increase of $N_{\rm tot}$ and the supercell volume with the chain length and cavity size, only the short chain C_6 within the relatively small cavity displayed in Figure 1 is accessible to accurate *ab-initio* simulations, without resorting to massively parallel supercomputers. To explore longer chains we resort to a slightly less

accurate but computationally far cheaper tight-binding (TB) model [30]. Appendix B reports a few technical details and a validation of the adopted TB model against *ab-initio* simulations.

Equilibrium Structures

We explore the insertion of three SPPCs with different lengths inside cavities of different axial lengths and radii, for a total of 6 prototype configurations. The cavity axial length is determined according to the rules discussed in section "The model". Table 2 lists the relevant structural parameters for the initial configurations.

Table 2: The structural parameters used to build the six different configurations considered in this section. m_a and m_c are the numbers of repeated lonsdaleite unit cell along the $\mathbf{a}, \mathbf{c}$ primitive vectors respectively; R is the cylindrical-cavity radius, m is the number of lonsdaleite c units defining the cavity height, and N is the number of atoms in the SPCC. The first row describes the structure of Figure 1. N_{tot}, Eq. (3), is the total number of atoms in the primitive cell of each configuration; N_{cyl}, Eq.(4), is the number carbon atoms that were removed in order to make room for the cavity.

$\mathbf{m_a}$	$\mathbf{m_c}$	**R** [pm]	**m**	**N**	$\mathbf{N_{tot}}$	$\mathbf{N_{cyl}}$
4	3	300	2	6	210	52
5	-	400	-	-	330	76
4	4	300	3	10	252	78
5	-	400	-	-	396	114
4	5	300	4	12	292	104
5	-	400	-	-	460	152

For all structures, we sample the electronic band structure in the Brillouin zone with a k-point mesh of the Monkhorst-Pack type [31], with a density of points larger than 17 nm^3. Starting from these initial structures based on ideal lonsdaleite, we relax each of them, minimizing the resulting total energy by means of a conjugate-gradient (CG) method, as implemented in the DFTB+ package [32,33], until the maximum force component acting on any atom decreases below 5×10^{-6} eV/Å. All these configurations and others mentioned below are relaxed to this precision level. In the relaxations, all atomic positions and the cell primitive vectors are allowed to change, to attain the optimized zero-pressure ($|P| < 10^5$ Pa) cell volume.

Table 3 summarizes the main results of these relaxations. Consider first

$$\Delta E = \frac{E_{\rm tot}}{N_{\rm tot}} - \frac{E_{\rm bulk}}{N_{\rm bulk}} \tag{5}$$

namely, the difference in the total adiabatic energy per atom of each structure, relative to that of perfect bulk lonsdaleite. The difference in binding energies ranges from 0.3 to 0.5 eV per atom, with a visible tendency to increase as the size of the cavity increases, involving more cut bonds.

Table 3: The energetics of the relaxed configurations: N fixes the length of the C_N chain, R is the cavity radius, and the other structural parameters are as listed in Table 2. ρ is the average density of the allotrope, systematically smaller than that of pure lonsdaleite, which is $\rho \simeq 3548.9$ kg/m^3 within the same DFTB model, to be compared with the experimental value $\rho \simeq 3510$ kg/m^3 [27]. ΔE is the difference in total energy per atom between the considered structure and bulk lonsdaleite. $E_{\rm cost}$, Eq. (6), is the energy required to cut the $N_{\rm surf}$ bonds, thus creating the cylindrical cavity. $E_{\rm gain}$ is on half of the energy lowering associated to the chain bonding to the inner cavity walls.

N	**R** [pm]	**a** [pm]	**c** [pm]	ρ [kg/m^3]	Δ**E** [eV]	$\mathbf{N}_{\rm surf}$	$\mathbf{E}_{\rm cost}$ [eV]	$\mathbf{E}_{\rm gain}$ [eV]
6	300	1006	1658	2884.0	0.35	38	3.64	3.70
	400	1256	1663	2917.4	0.33	50	3.81	3.23
10	300	1007	2082	2749.7	0.40	56	3.22	3.15
	400	1254	2084	2783.6	0.37	68	3.69	2.67
12	300	1007	2484	2669.5	0.43	74	3.03	2.71
	400	1257	249	2691.2	0.40	98	3.26	2.26

This result suggests that the dominant factor in the lower stability of these allotropes is the energy cost

$$E_{\rm cost} = \frac{E_{\rm cage} + E_{\rm cyl} - E_{\rm bulk}}{N_{\rm surf}} \tag{6}$$

required to cut the bonds and dig the appropriate cylindrical cavity out of bulk lonsdaleite. The three total adiabatic energies at the right hand side of Eq. (6), have the following meaning: $E_{\rm cage}$ is the energy of the lonsdaleite cage surrounding the cavity (no SPCC); $E_{\rm cyl}$ is the energy of the cylindrical portion of lonsdaleite that has been removed to create the cavity; and $E_{\rm bulk}$ is the energy of a portion of bulk lonsdaleite with the matching number of atoms $N_{\rm bulk} = N_{\rm cage} + N_{\rm cyl}$. All these energies refer to fully-relaxed configurations. $N_{\rm surf}$, also reported in Table 3, is the number of cut

bonds at the surface of the cylinder. Table 3 reports this energy per cut bond, which, as expected, is approximately constant as a function of the cavity size. Of course the number of cut bonds N_{surf} increases as the cavity size is increased, resulting in a progressive deterioration of the overall stability of the allotrope, observed in the increasing excess energy ΔE above.

On the other hand, the bonds of the SPCC with the cage are beneficial to the overall stability. We quantify this stabilizing contribution with

$$E_{\text{gain}} = \frac{E_{\text{cage}} + E_{\text{free } C_N} - E_{\text{tot}}}{2}, \tag{7}$$

namely the bonding energy (per bond) that is gained when attaching the SPCC inside the cavity. Here $E_{\text{free } C_N}$ is the energy of an unsaturated C_N SPCC isolated in vacuum.

The quantity E_{gain} depends on the stress state of the SPCCs, arising from the strain ε reported in Table 1. Indeed, according to that table, the C_6 and C_{12} SPCCs are strained by $\sim 9\%$, while for C_{10} buckles under a $\sim -1\%$ compressive strain. In this comparison, large strains ε decrease the bonding energy of the chain, as occurs for the C_6 and C_{12} configurations, due to the additional elastic-deformation contribution. The unexpected dependence of E_{gain} on the cavity radius R occurs as a consequence of the tendency of the surface layers of hexagonal carbon to graphitize and correspondingly bulge out inside the cavity, thus pressing the SPCC into buckling. This is an unphysical characteristic of the adopted TB model.

Thermal Stability

From the ground-state analysis of the previous subsection, we conclude that the SPCCs bound to the inside surface of a suitably sized cavity in lonsdaleite determine local minima of the adiabatic potential energy of carbon, which therefore represent stable allotropes. These allotropes are approximately 0.5 eV per atom less stable than lonsdaleite and other more stable forms of carbon, such as cubic diamond and graphite. Given a sufficiently long time, these metastable allotropes would eventually reconvert to one of the more stable ones. But how long would this spontaneous re-conversion take? In other words, can we predict how long a zayedene sample would remain sta-

ble at ordinary pressure and temperature conditions? This re-conversion process would certainly be initiated by the rupture of the SPCC component, followed by the conversion of sp carbon into sp^3 carbon, and concluded by a complicated sequence of re-crystallization steps.

Focusing on the earliest breaking step, a possible way to simulate the thermal stability of zayedene consists in analyzing the kinetics of the SPCC breaking reaction at high temperature and standard pressure. From the resulting high-temperature data it is possible to extrapolate the average lifetime of these allotropes down to room temperature.

For these simulations we use tight-binding molecular dynamics (TBMD) based on the force field given by the same TB Hamiltonian used for the structural characterization [30]. To control the temperature and pressure we use a Nosé-Hoover thermostat [34] and a Berendsen barostat [35]. We integrate the resulting molecular-dynamics equations of the NPT ensemble by means of the velocity-Verlet algorithm, as implemented in the DFTB+ package [32], with a 0.5 fs time step. We bring the system described in the first line of Table 2 to equilibrium at 1500 K and 1 bar and maintain it in these conditions for a $\simeq$ 15 ps-long run. From the final 5 ps of this evolution, we pick 7 groups of ten uncorrelated configurations each. The weak correlation is guaranteed by the time separation (at least 0.06 ps) between any two such configurations, longer than the decay time of the velocity autocorrelation function, evaluated for this same run to $\simeq$ 0.02 ps. The ten configurations selected for each group are separated by far longer times. Each group is then equilibrated at a different temperature: $T = 1500$, 1800, 2100, 2400, 2550, 2700, and 3000 K. For each temperature we simulate 10 samples differing only for their initial condition picked from the 1500 K run, as described above. The temperature of the $T = 3000$ K group is increased through an intermediate 2 ps equilibration step at 2550 K to prevent the SPCC from breaking immediately due to the explosive temperature increase.

After for each temperature we have obtained a set of independent fairly-well equilibrated configurations and velocities, we remove the thermostat and the barostat, and execute microcanonical fixed-volume (NVE) simulations, waiting for the SPCCs to break. This choice to get rid of the thermostat and barostat prevents the risk that the artifact atomic displacements induced by the Berend-

sen barostat may unphysically anticipate the breaking of a SPCC. The system size is large enough for the temperature and pressure to remain sufficiently well defined, even under microcanonical conditions. The rupture event is detected by means of a "marker" l which represents the length of the longest bond in the chain:

$$l = \max_{i=0\ldots N} |\mathbf{r}_i - \mathbf{r}_{i+1}| \,. \tag{8}$$

In this definition, for $i = 1,\ldots,N$, the $\mathbf{r}_i$ is the position of the i-th atom of the C_N SPCC. $\mathbf{r}_0$ and $\mathbf{r}_{N+1}$ represent the positions of the two cage atoms bound to SPCC extrema. To reduce the sensitivity to instantaneous fluctuations, we evaluate the average $\langle l \rangle$ over 100 fs. We define the SPCC to be broken when this average $\langle l \rangle$ exceeds 210 pm. This threshold sits just above the C-C bond inflection energy, and the validity range of the adopted TB model, see appendix B and in particular Figure 9.

The rupture time is taken as the first time step for which the $\langle l \rangle > 210$ pm condition is verified. Figure Figure 2 illustrates the evolution of the longest bond length as a function of the simulation time for four out of the ten simulations carried out for $T = 2100$ K. As the SPPC in independent samples rupture at some unpredictable random time under the effect of a thermal fluctuation, the overall "population" of yet unbroken SPCC is expected to decay exponentially in the time elapsed since the simulation beginning. The resulting population of remaining unruptured samples is represented by a stepwise decreasing function, Figure 3, starting from the initial number of independent samples, and decreasing by one each time a SPCC breaks. We fit this stepwise decreasing function with an exponential function $N_{\text{unruptured}} = N_0 \exp(-t/\tau)$ (dashed curves in Figure 3). Figure Figure 3 shows clearly that simulations at a higher temperature exhibit a more rapid decay of the unruptured SPCC population than the colder ones. 5 ps TBMD simulation runs are sufficient to evaluate this decay for all considered temperatures, except the lowest one, $T = 1500$ K, where, for a better accuracy we both triple the duration to 15 ps, and double the number of independent samples to 20 (reporting the population divided by 2 in Figure 3). In this way, all simulations last for a time

longer than or comparable with the relevant decay time τ. Figure Figure 3 shows these decays and fits for five out of the seven temperatures considered.

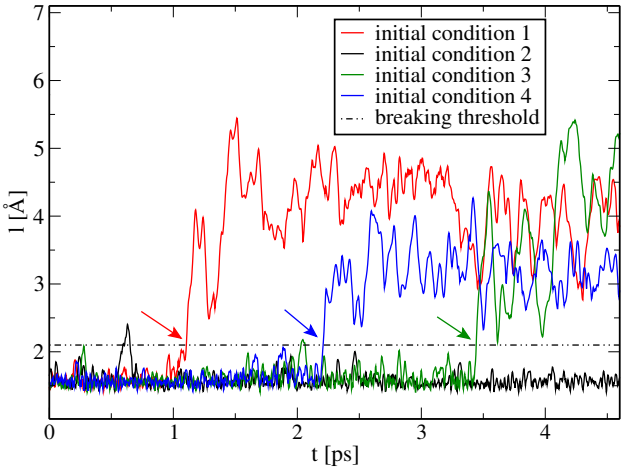

Figure 2: Four examples (out of 10) of the time dependence of the longest SPCC bond length l, defined in Eq. (8). Each curve reports an independent microcanonical simulation carried out starting with uncorrelated snapshots previously equilibrated at $T = 2100$ K. Arrows indicate the rupture times. Note that the spike of the black curve crossing the threshold is not recognized as a rupture event, thanks to averaging l: for the black-curve sample, the rupture is recognized to occur at a later time, not visible in this figure.

We can fit the temperature dependence of the decay rate τ^{-1} with an Arrhenius model:

$$\log(\tau^{-1}) = \log(A) - \frac{E_\mathrm{b}}{k_\mathrm{B}T} = a - \frac{T_\mathrm{b}}{T}\,. \tag{9}$$

Figure Figure 4 reports the decay rates τ^{-1} resulting from exponential fits of the stepwise decaying populations with errorbars representing the fit uncertainties. The data are arranged as a function of the inverse temperature, in order to compare with the Arrhenius relation (9). A weighted linear fit interpolates through these data. The weights are the inverse of the squared uncertainties on τ^{-1} obtained from the population fits. Table 4 reports the fitting coefficients, along with their standard deviations. The two pieces of information generated by this fit are the height of the energy barrier $E_\mathrm{b} = k_\mathrm{B}T_\mathrm{b}$ against SPCC rupture, and the thermal attempt rate A for this process. The resulting barrier is $E_b = (1.273 \pm 0.001)$ eV. Extrapolating Arrehnius formula down to 300 K, one obtains a best estimate of the room-temperature decay rate $\tau^{-1} \simeq (3.86 \pm 0.35) \times 10^{-7}$ s^{-1}, corresponding to a lifetime τ of the order of 1 month.

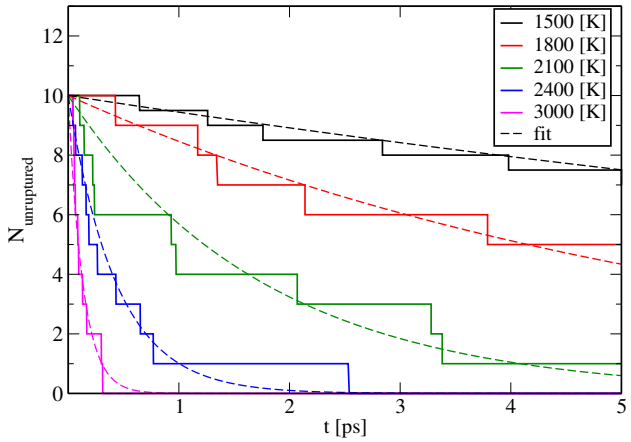

Figure 3: Solid lines: the time dependence of the population of unbroken SPCCs obtained executing, for each temperature T, 10 independent numerical simulations starting from uncorrelated initial conditions. The $T = 1500$ K case involves 20 independent simulations, for improved accuracy. Each time a SPCC breaks, a downward step occurs in the relevant curve. Dashed curves: the exponential fit of each population decay.

These results allow us to predict that in a hypothetical zayedene sample, containing a hugew number of SPCC, their unbroken number would steadily decay in time at a rate estimated by τ^{-1}. Given the approximations involved in the TB force field, discussed in appendix B, our numerical estimation of τ^{-1} cannot be relied upon quantitatively. As the barrier against rupture seem to be weaker in the TB model than in the more accurate DFT, we expect a longer room-temperature lifetime (i.e. smaller decay rate τ^{-1}) in reality than in our estimation. From a semi-quantitative point of view, our estimation agrees well with the observation of the slow decay of the fraction of sp carbon in nanostructured sp^2-sp^3 carbon: the SPCC fraction decays steadily over the course of months, if kept at room temperature under vacuum or in an inert-gas atmosphere [11,26,36-40].

Table 4: Best-fit values and standard deviation σ on the coefficients in the Arrhenius Eq. (9). The last column reports the relative uncertainties. The fit correlation coefficient $C_{a,T_b} = 0.972$.

coeff	value	standard deviation	std percentage
$a = \log(A)$ [$\log(s^{-1})$]	34.471	± 0.006	0.2%
$T_b = E_b/k_B$ [K]	14771	± 121	0.8%

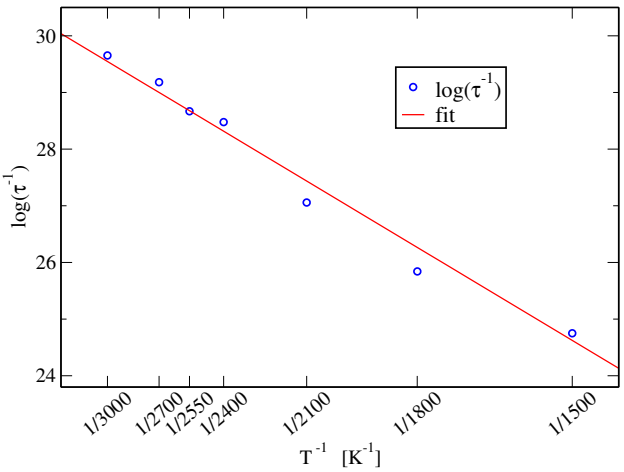

Figure 4: Points: the inverse lifetime τ^{-1} of the SPCC obtained from the fits of the decaying population of unruptured chains, as a function of the inverse temperature. The error bars are too small ($\simeq 0.01\%$) to be visible on the reported scale. Solid line: an Arrehenis fit of the lifetimes.

The Vibrational Spectrum

The vibrational eigenfrequencies could be obtained by means of the diagonalization of the dynamical matrix at the equilibrium point. However, for structures based on a minimum $N_{\mathrm{tot}} = 210$ atoms per cell, the individual modes are of limited interest, and one is more interested in the density of vibration frequencies. In particular, the characteristic high-frequency vibration frequencies of the SPCC can be used as a fingerprint to reveal their presence experimentally, for instance using Raman spectroscopy [1].

The density of vibration frequencies affects the correlations of specific dynamical quantities that can be obtained from a molecular dynamic (MD) simulation [41,42]. Specifically, the density of vibration frequencies $\rho(\omega)$ can be extracted from velocity autocorrelation functions computed according to the following equation:

$$\rho(\omega) = \frac{1}{3N_{\mathrm{at}}k_{\mathrm{B}}T}\int_{-\infty}^{\infty}\frac{\sum_{i=1}^{N_{\mathrm{at}}}\langle \mathbf{v}_i(t_0)\cdot\mathbf{v}_i(t_0+t)\rangle}{\sum_{i=1}^{N_{\mathrm{at}}}\langle \mathbf{v}_i(t_0)\cdot\mathbf{v}_i(t_0)\rangle}e^{i\omega t}\,dt\,, \tag{10}$$

where N_{at} is the total number of atoms in the investigate structure. This formula is evaluated by means the pwtools Python package [43]. Two difficulties affect the determination of the density of frequencies based on a MD simulation: anharmonic intermode interactions could distort the har-

monic normal frequencies; the initial condition can have the individual normal modes excited with randomly large or small intensities, thus leading to individual-mode contributions weighting differently and randomly in the spectrum. To mitigate the anharmonicity problem, it is sufficient to run the simulations at very small temperature: $T = 30K$. To alleviate the randomness of excitation, it is sufficient to average over many randomly chosen initial conditions, so that the energy gets evenly redistributed over the individual normal modes. In order to prevent any barostat- and/or thermostat-related frequencies, we simulate the system in the NVE ensemble.

We compute the velocity autocorrelations from 1-ps-long TBMD simulations, using as a starting points previously equilibrated runs at $T = 30$ K. This time duration is chosen to provide a frequency resolution of the order of $\Delta\nu \simeq 2/t_{\max} \simeq 2$ THz. The time step of the integration algorithm determines the highest frequency that can be resolved. With the adopted $\delta t = 0.5$ fs, the Nyquist limit frequency $0.5/\delta t = 1000$ THz stands safely above all possible vibrational frequencies, including the SPCC stretching modes, which reach up to 70 THz, or 2300 cm^{-1} at most [1]. To spread effectively the excitation over all normal-mode oscillators, we average ρ over 10 different uncorrelated configurations. Weak correlation is obtained by moving the atoms from their equilibrated positions with the addition of a random displacement uniformly distributed in the range $[-0.2;0.2]$ pm to each coordinate, and by resetting the initial atomic velocities to random values distributed according to the Maxwell-Boltzmann distribution at the simulated temperature.

Figure Figure 5 reports the density of normal-mode frequencies for three different structures: the zayedene of the first row of Table 2 repeated $2\times2\times2$ times along its primitive vectors, the corresponding lonsdaleite cage with the empty cylindrical cavities, and pure lonsdaleite represented by a $7\times7\times8$ repetition of its primitive cell. The zayedene and the SPCC-free cage produce qualitatively similar profiles. The main difference consists in the small but clearly visible peak around $\simeq 2200$ cm^{-1} which is only present in conjunction with the SPCC. We therefore attribute this peak precisely to vibrations concentrated on the SPCC inside the cavity, and, by comparison with past analysis [11,13,15,18-20,44] specifically to the SPCC stretching modes. Figure Figure 5 further shows that the presence of the cavity induces an increase in the density of frequencies below ap-

proximately 800 cm^{-1} at the expense of those above this wave number, compared to pure lonsdaleite. This is a consequence of the overall loss of rigidity that can be expected for a bulk crystal in which a regular array of cavities is created.

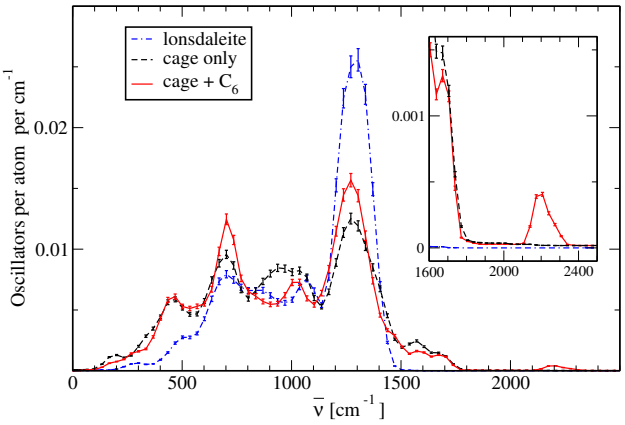

Figure 5: The density of vibrational frequencies obtained from the velocity autocorrelation, Eq. (10), for the following structures: pristine lonsdaleite (dot-dashed curve); lonsdaleite with a periodic array of cylindrical cavities, but no SPCC (dashed); the complete zayedene structure, consisting of $N_{\rm tot} = 210$ atoms per cell, as described in the first row of Table 2 (solid). The integral of each curve equals 3, the number of oscillators per atom. The frequencies near 2200 cm^{-1}, better visible in the inset, refer to the stretching modes of the SPCC.

Electronic Properties

To investigate the electronic structure of the simplest allotrope, that of the first row of Table 2, beside TB, we also we perform *ab-initio* DFT simulations, using the SIESTA package [45]. For the exchange correlation energy, we consider a generalized gradient approximation (GGA), the Perdew-Burke-Ernzerhof functional [46], and expand the electronic wave functions on a standard basis for carbon made by double-ζ radial wave function and polarization orbitals (DZP) , as implemented in SIESTA [45]. We sample the $\mathbf{k}$ points with a $3 \times 3 \times 4$ Monkhorst-Pack mesh[31]. Like in the TB model, we optimize the structure with a variable-cell relaxation CG method, until the forces are converged to the same accuracy adopted in the TB simulations, $< 10^{-4}$ eV/Å. The final structure agrees well with the one obtained in the TB model, see appendix B. For the relaxed configuration see section Supporting Information File 1.

For this relaxed structure, we compute the electronic bands, and the resulting total density of states (DOS), plus a few projected DOS that allow us to characterize the electronic properties of this allotrope. As confirmed by a detailed comparison between the band structure of pure lonsdaleite computed with DFT and with TB, the latter does not reproduce especially accurately the electronic properties of hexagonal diamond, with significant deviations especially in the region of the empty states. In particular, for lonsdaleite TB foresees a direct band gap at the center of the first Brillouin zone, rather the smaller indirect gap predicted by the *ab initio* method. For this reason, of the zayedene allotrope, we report only the more reliable DFT band structure, rather than the TB one. Figure Figure 6 shows the electronic band structure evaluated along the standard path reported on the horizontal axis. Figure Figure 7 reports the corresponding DOS. The metallic character of this allotrope is evident in both figures. Two flat bands cross the Fermi level, certainly originated by the dangling bonds inside the cavity. To verify whether also the SPCC contributes to the metallicity of the structure or not, we evaluate the projected density of states (PDOS) on the SPCC and on the atomic orbitals of the cage. The PDOS $g_\mu(\varepsilon)\,dE$ counts the number of Kohn-Sham states having energy in the range E and $E+dE$, weighted by their overlap with a given atomic orbital μ:

$$g_\mu(E) = \frac{1}{N_\mathbf{k}} \sum_{i}^{bands} \sum_{\mathbf{k}} \sum_{\nu} c^*_{\nu,i}(\mathbf{k}) c_{\mu,i}(\mathbf{k}) S_{\nu,\mu}(\mathbf{k}) \delta(E - E_i(\mathbf{k}))\,. \tag{11}$$

Here $c_{\mu,i}(\mathbf{k})$ is the coefficient of the projection of the $\psi_i(\mathbf{k})$ Kohn-Sham wave function with eigenenergy $E_i(\mathbf{k})$ on the μ-th atomic orbital; $S_{\nu,\mu}(\mathbf{k})$ is the superposition matrix of the atomic basis. We replace the delta function with a Gaussian with width $\sigma = 0.15$ eV. For the DOS calculations we employ a $15 \times 15 \times 15$ grid of $\mathbf{k}$ points, after verifying that it produces results essentially identical to a $10 \times 10 \times 10$ grid. The DOS of a specific set α of atoms is then simply the sum of the PDOS relative to every orbital of every atom in that set: $g_\alpha(E) = \sum_{\mu \in \alpha} g_\mu(E)$. If the set α coincides with the entire primitive cell, then $g_\alpha(E)$ coincides with the total DOS $g(E)$.
Figure Figure 7 reports three PDOS, along with the total one. Given the small fractional number of atoms in the SPCC, their contribution to the total DOS is relatively small. In particular, we note that around the Fermi level E_F there is little or no contribution of the SPCC orbitals. In contrast,

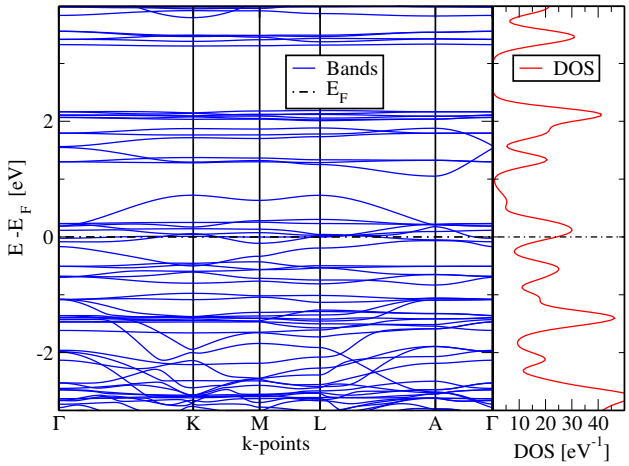

Figure 6: The band structure of the zayedene allotrope evaluated along a standard path in k space. The Fermi level is represented by the dot dashed line. The metallic character results from the two bands crossing the Fermi level E_F; the flat bands around E_F involve both the cavity dangling bonds and the SPCC.

the contributions of the atoms forming the cavity surface are dominant around E_F. This decomposition proves that the metallic behavior of this allotrope arises due to the cage dangling bonds, and not because of the presence of the SPCC. Accordingly, even though this result holds for this specific zayedene, we can predict that if one computed the bandstructure of any crystal of this type, one would find a qualitatively similar situation: extremely flat bands crossing the Fermi level associated to the cavity dangling bonds. The metallicity of such narrow flat bands is fragile against disorder [47,48], electron-electron correlation [49], and electron-phonon[50] coupling: all these effects would tend to destroy the metallic state in a real-life sample. As a result, while a very pure and defect-free sample of this specific zayedene may indeed turn out to be metallic, it is likely that similar allotropes characterized by a longer periodicity (more rarefied cavities, with a smaller sp fraction) and/or poorer crystal quality behave as insulators, or very bad metals, or possibly even superconductors.

Discussion and conclusions

In this work we propose a possible scheme for the inclusion of SPCCs in bulk sp^3 carbon. For the host, we consider hexagonal diamond. Similar results are to be expected for cubic diamond. By

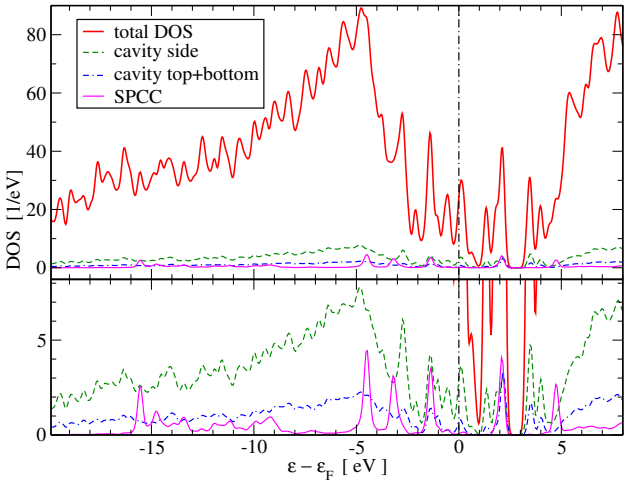

Figure 7: The total DOS of the simplest zayedene (solid red curve), resolved in the contributions arising from the projections on the C_6 SPCC (solid violet), and on different portions of the cavity surface (dashed and dot-dashed). The Fermi level is represented by the vertical dot-dashed line. The lower panel amplifies the PDOS signal, clarifying that the metallic bands consist mainly of dangling bonds at cavity surface atoms, with negligible contribution of the SPCC.

building a regular array of cavities, we construct a crystalline cage where SPCCs bind naturally at their ends, and are kept isolated from each other and from the external environment.

Using a TB model we analyze the structural and binding properties of several different combinations of SPCCs of different lengths with cavities of different diameters, obtaining a general dependence of the SPCC stability on its stress state. For the simplest structure, by means of high-temperature MD simulations, we investigate the effects stability against the SPCC rupture. The kinetics of the chain-rupture reaction allows us to predict a room-temperature lifetime in the months region, similar to what is observed experimentally for sp-sp^2 combinations [1].

The vibrational frequencies, computed by means of velocity autocorrelation functions in low-temperature MD simulations, allow us to identify a high-frequency peak around 2200 cm^{-1} as the fingerprint of the SPPC. We predict that such a peak should be visible in IR or Raman spectroscopy. Its intensity should also allow one to estimate the concentration of cavities with SPCCs in the sample.

For the electronic properties for the simplest allotrope, we resort to accurate *ab-initio* DFT simulations. The obtained band structure and corresponding DOS prove, on one hand, that these allotropes are metallic and, on the other hand, that the narrow metallic bands are associated with

the dangling bonds of the cavity surface. The SPCC orbitals do not contribute significantly to the metallic character.

The presence of very narrow bands at the Fermi level, suggests that zayedene structures could provide an interesting playground for materials science, where the interplay of electron-electron correlation, electron-phonon coupling, and disorder may lead to several competing metallic, insulating, and possibly even superconductive states, in a potentially rich phase diagram. For these reasons, it would be quite interesting to synthesize and characterize one or more of these allotropes in the lab. This same strategy of inserting SPCCs in suitable cavities could prove useful even outside the carbon-only concept. More general scenarios worth pursuing as well, include the insertion or growth of SPCCs inside cavities e.g. in silicon or germanium clathrates [51-53].

Appendices

Appendix A: Extra configurations

Besides the length of the chain and the cavity dimensions, the zayedene structure is defined by one more degree of freedom: the orientation of the SPCC relative to the cavity axis. We assume, as in the previous analysis, that the chain ends bind to undercoordinated carbon atoms sticking out toward the inside of the cavity. Figure Figure 8f provides the labeling of these carbons. Changing these binding sites, we construct five more initial configurations for a C_6 inside a $R = 300$ pm and $m = 2$ cavity. Starting with straight (oblique, when relevant) geometries of the SPCC, we carry out full relaxations in TB, the same level of theory as for the results reported in section "Numeric simulations".

Table 5: The difference in the total adiabatic energy per atom of each structure, relative to the C-C structure with both sides of the SPCC attached to the central binding sites, as in Figure 1. $\delta E = (E_S - E_{C-C})/N$, where the label S identifies the pair of binding sites, see Figure 8.

binding sites	**C − S1**	**S1 − S2**	**S1 − S3**	**S1 − S4**	**S1 − S1**
δ**E** [meV]	0.0	3.3	−11.9	−15.6	−8.3

Panels a-e of Figure Figure 8 report side views of the resulting relaxed configurations, marking the

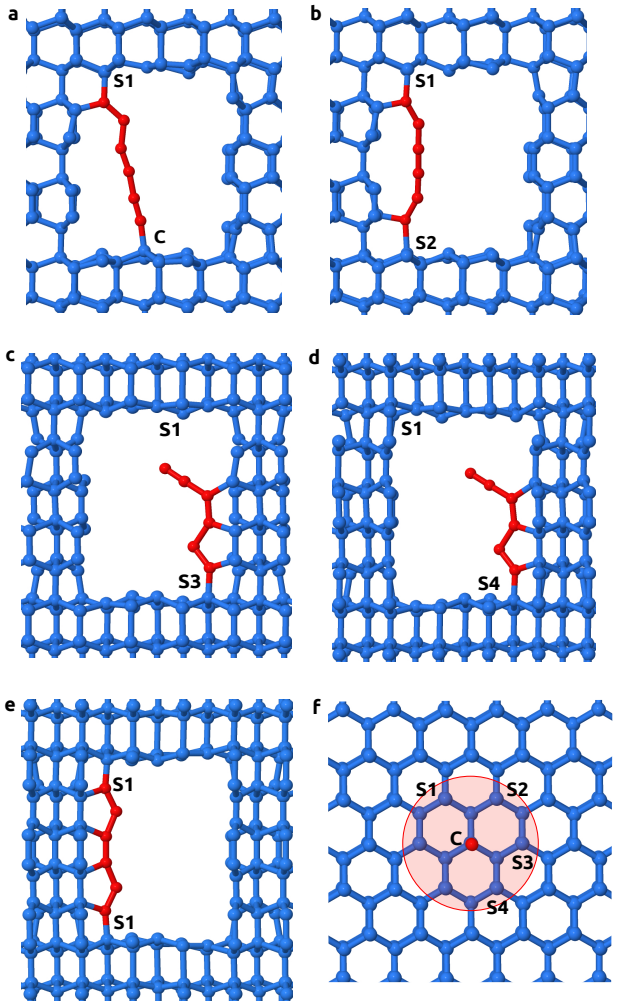

Figure 8: A few extra possible relaxed arrangements of the C_6 SPCC in a lonsdaleite-based cage. Panels **a**-**e** report TB-relaxed configurations. In each example the atoms at the chain ends start of bound to different cage carbons sites sticking out inside the cavity, labelled with $S1 \ldots S4$ as indicated in panel **f**.

binding sites taken at the beginning of relaxation. Table 5 reports the difference δE in energy per atom, relative to the center-center (C-C) configuration investigated in the main text. The oblique $S1 - C$ and $S1 - S2$ arrangements reported in Figure 8a,b are energetically almost equivalent to the C-C one. In these configurations a sizable fraction of the SPCC retains its *sp*-character. The other three arrangements ($S1 - S3$, $S1 - S4$ and the vertical $S1 - S2$) are energetically favorable. This is clearly originated by the chain rebinding to the cavity side. This energy lowering would be even larger if all the SPCC atoms did reconstruct properly to lonsdaleite. Instead, the CG mini-

mization leads to frustrated arrangements including pentagonal carbon rings, which could probably be healed if a further simulated annealing was carried out.

The main message of these relaxations is that SPCCs are indeed unstable against re-conversion to sp^2 or sp^3 carbon. As a consequence, to keep them isolated and prevent this re-conversion from occurring, one needs to place the SPCCs near the central axis in cavities of sufficiently large lateral size. The possibility to arrange SPCCs perpendicularly to the **c** axis is likely to generate even more allotropes which may deserve further investigation.

Appendix B: Validation of the method

The TB method joins the advantage of describing the electrons, and therefore bonding and multiple hybridizations, to the price of a higher computational cost compared to fully classical potentials, but still far cheaper than a fully *ab-initio* approach.We adopt a TB method in a density-functional-based formulation, the DFTB [33]. We use a TB parameterization that has been reported to reproduce the structural and mechanical properties of sp^3 carbon quite accurately [54,55], as implemented in the DFTB+ package [32].

In view of the utilization of this TB force field for the present work, we need to verify how well it performs for SPCCs. For this purpose, we compare the dependence of the total energy of a C_{12} SPCC isolated in vacuum on the length of its central bond, from a shorter-than equilibrium spacing, until full decomposition into 2 C_6 SPCCs. We take as reference DFT-GGA as implemented in SIESTA (Perdew-Burke-Ernzerhof functional [46], DZP basis)[45]. In Figure 9, we compare the resulting *ab-initio* adiabatic potential with the homologous TB curves, as obtained by means of the DFTB+ implementation [32]. In the context of these periodic codes, we simulate an isolated molecular SPCC by aligning it along the **c** axis of an elongated tetragonal cell, with $c = 4$ nm (much longer than the SPCC length), and $a = 0.5$ nm (greater than the cutoff distance for C-C interactions). In all calculations, while keeping the length of the central bond fixed, all other atoms are left free to relax to their equilibrium positions. For each curve, the reference energy is the energy of two unconnected isolated relaxed C_6 chains.

The reference DFT-GGA curve grows smoothly on both sides of a minimum near 130 pm, and reaches saturation to its infinite-distance value around 280 pm. The two TB curves report the result of calculations done without any charge correction (dashed line), and the outcome of the TB model when properly taking into account second-order fluctuations in electron charge density computed self consistently (self-consistent charge, or SCC, dot-dashed) [33]. This comparison allows us to check whether the Coulombic interactions among electrons, which are not explicitly considered in a conventional TB approach, are important to improve the energetics of the system.

The compared models show a general semi-quantitative agreement up to $\simeq$ 220 pm, but beyond this separation the TB approximation fails to describe dissociation reliably. Overall, the TB model tends to underestimate the bond energy ($\sim$ 6 eV rather than $\sim$ 8 eV). A few extra significant differences occur nearing dissociation, as shown in Fig Figure 9. TB fails significantly for high strain of the central bond. DFT-GGA describes the expected smoothly attractive profile near dissociation. In contrast the non-SCC TB model exhibits a level crossing to a dissociative state above 225 pm. More seriously, the asymptotic limit is incorrect, because an unphysical charge transfer between the two C_6 moieties leads, at high separation, to a total energy lower than twice that of a single isolated C_6! SCC corrections have a significant effect in correcting the high-strain region, smoothing out the level crossing, and suppressing the unphysical charge transfer, and leading therefore to the correct large-distance asymptote, while still foreseeing an incorrect dissociative regime above 230 pm.

Due to the unsaturated carbons, the molecular C_{12} dissociation studied here should be considered as a worst-case scenario. In the calculations we carry out for our carbon structures, the bond saturation of all *sp* carbon prevents the formation of such unphysical charged states, leading to far better reliability of the TB model, even in its plain (no SCC) faster incarnation, which we adopt throughout. The only significant problem that we recognize in the adopted TB model stands in its spontaneous tendency to convert the (001) surface layer of lonsdaleite from sp^3 to sp^2, which would become problematic if we wanted to address larger cavities.

The reliability of the TB model for the simulation of these allotropes is verified also by comparing

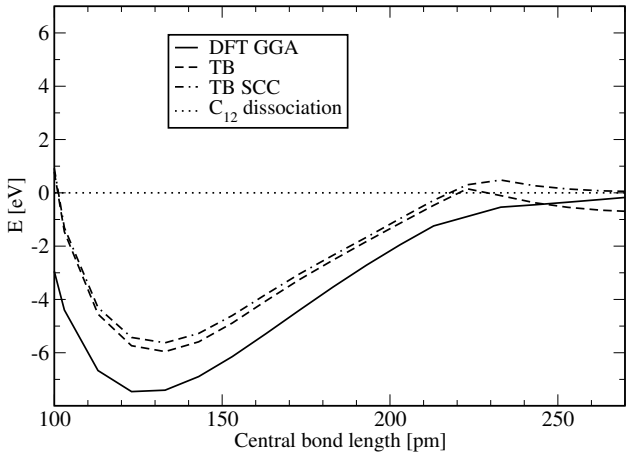

Figure 9: Comparison of the binding energy curves of a C_{12} chain $\rightarrow$ 2 C_6 chains, as a function of the length of the central bond (with all other bonds being left free to relax) obtained with the different models considered in the present paper. Solid line: reference calculation, the accurate DFT-GGA obtained by means of the SIESTA package [45]; dashed line: one-shot TB, no charge self consistency; dot-dashed line: self-consistent charge TB (TB-SCC). For all curves, the zero reference energy (dotted) is taken as twice the energy of an isolated C_6 chain.

the predictions for the simplest zayedene, a C_6 chain inserted in a $R = 3$ Å, $m = 2$ cavity, namely the structure described in the first row of Table 2 and in Figure 1. Table 6 compares the predictions of the structural properties and energetics for this allotrope obtained with the TB models with the DFT-GGA reference. Both TB and TB-SCC relaxations give cell parameters vectors **a** and **c** in agreement with the DFT-GGA ones within some 10 pm. SPCC individual bond lengths are within 2 pm. We provide the DFT fully-relaxed structure as Supplementary Material.

Table 6: Structural properties of the C_6 chain inside the $R = 300$ pm, $m = 2$ cavity, namely the structure of Figure 1 and of the first row of Table 2. a, c are the fully-relaxed lengths of the hexagonal cell primitive vectors; d^i_{CC} are the lengths $d^i_{\mathrm{CC}} = |\mathbf{r}_i - \mathbf{r}_{i-1}|$ of successive bonds in the SPCC, with the same definition as for Eq. (8); the energy per atom ΔE is defined in Eq. (5).

	a [pm]	**c** [pm]	$\mathbf{d}^1_{\mathrm{CC}}$ [pm]	$\mathbf{d}^2_{\mathrm{CC}}$ [pm]	$\mathbf{d}^3_{\mathrm{CC}}$ [pm]	$\mathbf{d}^4_{\mathrm{CC}}$ [pm]	Δ**E** [eV]
DFT-GGA	997	1646	146.6	123.3	137.0	124.4	0.345
TB	1006	1658	145.4	121.8	136.6	121.7	0.350
TB SCC	1005	1661	147.4	121.6	138.1	122.3	0.373

Also the energy cost needed to create these structures starting from bulk lonsdaleite is quite close to the DFT-GGA reference prediction.

TB slightly overestimates the instability of the structure, interestingly with SCC performing a little

bit worse than much faster non-SCC TB. According to these observations, we conclude that all binding energies based on the adopted TB model tend to underestimate slightly the local stability of these allotropes, but are quite reliable for their semi-quantitative investigation.

Supporting Information

Supporting information features one single file containing the relaxed configuration of the C_6 zayedene defined by the first row of Table 2 and relaxed by means of *ab-initio* simulations.

Supporting Information File 1:

File Name: C6_zayedene.exyz

File Format: extended xyz

Title: C6 zayedene

Acknowledgments

The authors wish to acknowledge computing support from the CINECA supercomputing national center, and from the INDACO computing infrastructure of the University of Milano. FD and NM acknowledge useful discussion with Giovanni Onida.

References

1. Casari, C.; Milani, A. *MRS Commun.* **2018**, *8*, 207–219. doi:10.1557/mrc.2018.48.

2. Prazdnikov, Y. *J. Mod. Phys.* **2010**, *02*, 845–848. doi:10.4236/jmp.2011.28100.

3. Cretu, O.; Botello-Mendez, A. R.; Janowska, I.; Pham-Huu, C.; Charlier, J.; Banhart, F. *Nano Lett.* **2013**, *13*, 3487–3493. doi:10.1021/nl4018918.

4. Jin, C.; Lan, H.; Peng, L.; Suenaga, K.; Iijima, S. *Phys. Rev. Lett.* **2009**, *102*, 205501.

5. Zanolli, Z.; Charlier, J.-C. *Phys. Rev. B* **2010**, *81*, 165406.

6. Shi, L.; Rohringer, P.; Wanko, M.; Rubio, A.; Waßerroth, S.; Reich, S. e. a. *Phys. Rev. Materials* **2017**, *1*, 075601. doi:10.1103/PhysRevMaterials.1.075601.

7. Kotrechko, S.; Timoshevskii, A.; Kolyvoshko, E.; Matviychuk, Y.; Stetsenko, N. *Nanoscale Res. Lett.* **2017**, *12*, 327.

8. Smith, P. P. K.; Buseck, P. R. *Science* **1982**, *216*, 984–986. doi:10.1126/science.216.4549.984.

9. *Polyynes: Synthesis, Properties, and Applications*; Cataldo, F., Ed.; CRC, Taylor&Francis, London, 2005.

10. Bogana, M.; Colombo, L. *Appl. Phys. A* **2007**, *86*, 275.

11. Ravagnan, L.; Manini, N.; Cinquanta, E.; Onida, G.; Sangalli, D.; et al., C. M. *Phys. Rev. Lett.* **2009**, *102*, 245502.

12. Cahangirov, S.; Topsakal, M.; Ciraci, S. *Phys. Rev. B* **2010**, *82*, 195444.

13. Onida, G.; Manini, N.; Ravagnan, L.; Cinquanta, E.; Sangalli, D.; Milani, P. *Phys. Status Solidi B* **2010**, *247*, 2017.

14. Zeng, M. G.; Shen, L.; Cai, Y. Q.; Sha, Z. D.; Feng, Y. P. *Appl. Phys. Lett.* **2010**, *96*, 042104.

15. Cataldo, F.; Ravagnan, L.; Cinquanta, E.; Castelli, I. E.; Manini, N.; Onida, G.; Milani, P. *J. Phys. Chem. B* **2010**, *114*, 14834.

16. Ataca, C.; Ciraci, S. *Phys. Rev. B* **2011**, *83*, 235417.

17. Erdogan, E.; Popov, I.; Rocha, C. G.; Cuniberti, G.; Roche, S.; Seifert, G. *Phys. Rev. B* **2011**, *83*, 041401.

18. Cinquanta, E.; Ravagnan, L.; Castelli, I. E.; Cataldo, F.; Manini, N.; et al., G. O. *J. Chem. Phys.* **2011**, *135*, 194501.

19. Castelli, I. E.; Ferri, N.; Onida, G.; Manini, N. *J. Phys.: Condens. Matter* **2012**, *24*, 104019.

20. Cinquanta, E.; Manini, N.; Ravagnan, L.; Caramella, L.; Onida, G.; et al., P. M. *J. Chem. Phys.* **2014**, *140* (24), 244708–244714.

21. Casari, C.; Bassi, A. L.; Ravagnan, L.; Siviero, F.; Lenardi, C.; et al., P. P. *Phys. Rev. B* **2004**, *69*, 075422.

22. Liu, M.; Artyukhov, V. I.; Lee, H.; Xu, F.; Yakobson, B. I. *ACS Nano* **2013**, *7 11*, 10075–82. doi:10.1021/nn404177r.

23. Banhart, F. *Beilstein J. Nanotechnol.* **2015**, *6*, 559–569. doi:10.3762/bjnano.6.58.

24. Ataca, C.; Ciraci, S. *Phys. Rev. B* **2011**, *83*, 235417. doi:10.1103/PhysRevB.83.235417.

25. Chuvilin, A.; Meyer, J. C.; Algara-Siller, G.; Kaiser, U. *New J. Phys.* **2009**, *11*, 083019.

26. Castelli, I. E.; Salvestrini, P.; Manini, N. *Phys. Rev. B.* **2012**, *85*, 214110.

27. Bundy, F. P.; Kasper, J. S. *J. Chem. Phys* **1967**, *46*, 3437–3446. doi:10.1063/1.1841236.

28. He, H.; Sekine, T.; Kobayashi, T. *Appl. Phys. Lett.* **2002**, *81*, 610–612. doi:10.1063/1.1495078.

29. Woodcock, H. L.; Schaefer, H. F.; Schreiner, P. R. *J. Phys. Chem. A* **2002**, *106*, 11923.

30. Laasonen, K.; Nieminen, R. *J. Phys. Condens. Matter* **1990**, *2*, 1509–1520. doi:10.1088/0953-8984/2/6/010.

31. Monkhorst, H.; Pack, J. D. *Phys. Rev. B* **1974**, *13*, 5188.

32. Aradi, B.; Hourahine, B.; Frauenheim, T. *J. Chem. Phys. A* **2007**, *111*, 5678–5684.

33. Koskinen, P.; Mäkinen, V. *Comput. Mater. Sci.* **2009**, *47*, 237–253.

34. Evans, D. J.; Holian, B. L. *J. Chem. Phys.* **1985**, *83*, 4069.

35. Berendsen, H. J. C.; Postma, J. P. M.; van Gunsteren, W. F.; Di Nola, A.; Haak, J. R. *J. Chem. Phys.* **1984**, *81*, 3684–3690. doi:10.1063/1.448118.

505 36. Ravagnan, L.; Siviero, F.; Lenardi, C.; Piseri, P.; Barborini, E.; Milani, P. *Phys. Rev. Lett.*
506 **2002**, *89*, 285506.

507 37. Weimer, M.; Hieringer, W.; Sala, F. D.; Gorling, A. *Chem. Phys.* **2005**, *309*, 77.

508 38. Innocenti, F.; Milani, A.; Castiglioni, C. *J. Raman Spectrosc.* **2010**, *41*, 226.

509 39. Ravagnan, L.; Mazza, T.; Bongiorno, G.; Devetta, M.; Amati, M.; et al., P. M. *Chem. Com-*
510 *mun.* **2011**, *47*, 2952.

511 40. Zhang, G. P.; Fang, X. W.; Yao, Y. X.; Wang, C. Z.; Ding, Z. J.; Ho, K. M. *J. Phys.: Condens.*
512 *Matter* **2011**, *23*, 025302.

513 41. Lee, C.; Vanderbilt, D.; Laasonen, K.; Car, R.; Parrinello, M. *Phys. Rev. B* **1993**, *47*, 4863.

514 42. Meyer, R.; Comtesse, D. *Phys. Rev. B* **2011**, *83*, 014301. doi:10.1103/PhysRevB.83.014301.

515 43.

516 44. Cinquanta, E.; Manini, N.; Ravagnan, L.; Caramella, L.; Onida, G.; Milani, P.; Rudolf, P. *J.*
517 *Chem. Phys.* **2014**, *140*, 244708.

518 45. Soler, J. M.; Artacho, E.; Gale, J.; García, A.; Junquera, J.; et al., P. O. *J. Phys. Condens. Mat-*
519 *ter* **2002**, *14*, 2745.

520 46. Perdew, J.; Burke, K.; Ernzerhof, M. *Phys. Rev. Lett.* **1996**, *77*, 3865.

521 47. Byczuk, K.; Hofstetter, W.; Vollhardt, D. *Phys. Rev. Lett.* **2005**, *94*, 056404. doi:10.1103/
522 PhysRevLett.94.056404.

523 48. et al., M. H. A. *Science* **1995**, *269*, 198.

524 49. Yanagisawa, M. M., T.; Yamaji, K. *J. Appl. Math. Phys.* **2014**, *2*, 72–76. doi:10.4236/jamp.
525 2014.25010.

526 50. Krätschmer, W. *Nanostruct. Mater.* **1995**, *6*, 65 –72. doi:https://doi.org/10.1016/
527 0965-9773(95)00030-5.

528 51. Kawaji, H.; Horie, H.; Yamanaka, S.; Ishikawa, M. *Phys. Rev. Lett.* **1995**, *74*, 1427.

529 52. Yamanaka, S. *Dalton Trans.* **2010**, *39*, 1901.

530 53. Dolyniuk, J.; Owens-Baird, B.; Wang, J.; Zaikina, J. V.; Kovnir, K. *Mater. Sci. Eng. R* **2016**,
531 *108*, 1.

532 54. Köhler, C.; Frauenheim, T. *Surf. Sci.* **2006**, *600*, 453 –460. doi:https://doi.org/10.1016/j.susc.
533 2005.10.044.

534 55. Rauls, E.; Elsner, J.; Gutierrez, R.; Frauenheim, T. *Solid State Commun.* **1999**, *111*, 459 –464.
535 doi:https://doi.org/10.1016/S0038-1098(99)00137-4.